ARCHIVES OF ELECTRICAL ENGINEERING VOL. 69(2), pp. 467–481 (2020)

DOI 10.24425/aee.2020.133038

Analysis of IPM motor parameters in an 80-kW traction motor

ADRIAN MŁOT[1], MARCIN KOWOL[1], JANUSZ KOŁODZIEJ[1], ANDRZEJ LECHOWICZ[1], PIOTR SKROBOTOWICZ[2]

[1] *Politechnika Opolska*
Poland

[2] *Auto Power Electronic*
Opole, Poland
e-mail: a.mlot@po.edu.pl

(Received: 28.11.2019, revised: 11.02.2020)

Abstract: This paper presents a review of the electromagnetic field and a performance analysis of a radial flux interior permanent magnet (IPM) machine designed to achieve 80 kW and 125 Nm for an electric and hybrid traction vehicle. The motor consists of a 12-slot stator with a three-phase concentrated winding as well as an 8-pole rotor with V-shaped magnets. Selected motor parameters obtained from an IPM prototype were compared with the design requirements. Based on the electromagnetic field analysis, the authors have indicated the parts of the motor that should be redesigned, including the structure of the rotor core, aimed at enhancing the motor's performance and adjusting segmentation for magnet eddy current loss reduction. In addition, iron and PM eddy current losses were investigated. Moreover, transient analysis of current peak value showed that the current may increase significantly compared to steady-state values. A map of transient peak current load vs. torque load plotted against rotor speed was provided. Based on the numeric and analytical results of physical machine parameters, the authors indicate that collapse load during the motor's operation may significantly increase the risk of permanent magnet (PM) demagnetization. It was also found that collapse load increases the transient torque, which may reduce the lifetime of windings.

Key words: electromagnetic review, electric vehicle, IPM motor, permanent magnet brushless motor, radial flux permanent magnet motor, V-shaped interior permanent magnet

1. Introduction

The radial flux brushless AC interior permanent magnet (IPM) motor presented in this paper was designed for propulsion drives in electric vehicles (EVs) [1–5]. The IPM motor was designed

for distributed drive electric vehicles in which the chassis of the EV consists of a front- and rear-wheel independent drive type, with an arrangement of PM synchronous motors for driving the rear and front wheels [6–8]. The main benefits of a distributed drive electric vehicle system were described in [1]. The 80-kW prototype presented here is intended for the front and rear drives. The motor was designed to achieve a nominal torque of 125 Nm; the nominal speed is 4500 rpm at 113 V induced per winding phase. The IPM prototype (prior to its being mounted on the test rig) and main machine dimensions are shown in Fig. 1.

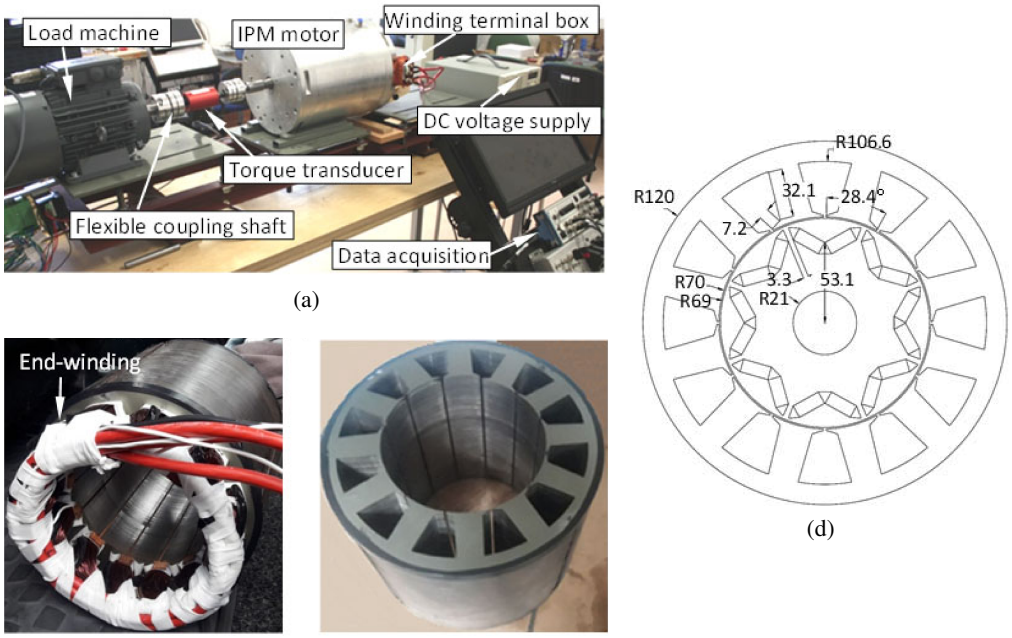

Fig. 1. IPM motor prototype (80 kW) prior to its being mounting on the test rig (a); stator with concentrated winding (b); laminated stator core (c); main IPM motor dimensions (the dimensions of flux barrier are not presented here) (d)

The prototype of the IPM motor consists of permanent magnets inserted within the laminated rotor core and the conventional three-phase concentrated winding of a stator. The stator lamination and rotor lamination are presented in Fig. 2. The PM V-shape formed from the laminated structure of the rotor represents a single pole of the rotor. The size and the angle between V-shaped PMs give the advantages of high torque constant, the requisite low cogging torque, and a simple structure. The use of simple rectangular magnet blocks reduces machining costs [9–11].

Moreover, it is crucial to properly design the magnetic flux barrier in order to obtain the required flux paths between the rotor, air gap, and stator, and to reduce flux leakage to a minimum [12–16]. The shape of the magnetic flux barrier in the rotor is simple and provides acceptable flux density distribution around this barrier. The flux passing the 1-mm air gap assures low total harmonic distortion of back electromotive force (B-EMF).

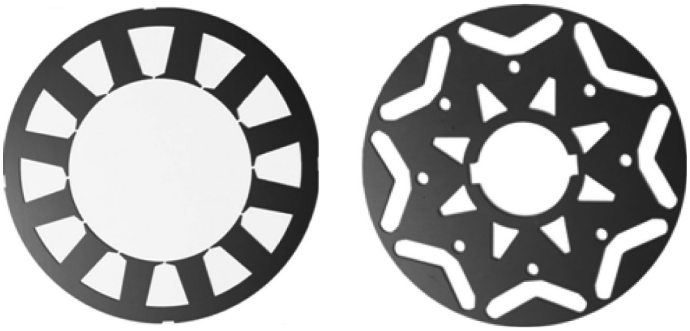

(a) (b)

Fig. 2. Thin lamination sheet of the stator (a) and rotor (b) as a steel portion of the IPM motor (the lamination sheets are not scaled)

The main IPM motor prototype parameters are listed in Table 1.

Table 1. The main IPM motor parameters and material specifications

Motor element	Description	Value	Unit
Winding type	Concentrated, double-side	–	–
Number of coils per chase	Connected in parallel	4	–
Number of turns per coil	–	18	–
Phase resistance	–	4.3	mΩ
Magnet material and type	NdFeB, N33EH	–	–
Number of magnet segment in axial direction	Per pole	6	–
Steel material (rotor, stator)	M270–35A	–	–
Number of slots per rotor pole	–	12/8	–
Magnet height/width	–	8.6/19	mm/mm
Active motor length	–	180	mm

Comparison between the data from the simulation and experiment involving the B-EMF, cogging torque and electromagnetic static torque show a sufficient degree of agreement. The measured IPM motor parameters are compared against the finite element computations (finite element model is described in next section) and listed in Table 2. The shaft of the motor prototype is directly coupled to a flexible coupling via an in-line torque transducer, then to the next flexible coupling and to the load machine (see Fig. 1(a)). The measurements were conducted by application of a test-stand (Fig. 1(a)) consisting of an IPM prototype, torque transducer, two flexible coupling shafts, an AC load machine, and a multichannel high-resolution data acquisition system. The motor phase voltage is monitored directly on the exit of the phase winding terminal by the data acquisition system. During an open-circuit test, the amplitude of the voltage waveform induced in a single phase, and the peak of the cogging torque waveform at low speed operation are determined and

listed in Table 2. Moreover, the peak of the static electromagnetic torque was determined from the monitored torque waveform during load operation condition (the armature winding supplied by DC current).

Table 2. Measurements compared with numerical model based on 2-D FEA

Motor parameter	Value as measured	Value as computed FEA	Unit
Peak cogging torque	1	0.96	Nm
Amplitude of first order harmonic of voltage induced in single phase at 1000 rpm	31	30	V
Peak electromagnetic static torque at I = 30 A	15.6	14.03	Nm

A brief review of the electromagnetic field and useful machine parameters is presented in the next section. It is very important to analyze the complex loss mechanism of harmonic and slotting effects, because the losses can significantly affect the IPM motor's performance. The authors investigate the loss of eddy currents within magnets, a rotor, and stator cores at low and high speeds [17]. Copper loss was omitted in this paper. Additionally, the risk of demagnetization following collapse load is investigated. The finding is presented in this paper, and will be applied to the next IPM motor prototype. Moreover, the findings may also be very useful for motor design engineers.

2. Electromagnetic review

Fig. 3 presents two- and three-dimensional (2D, 3D) magnetostatic and transient numerical models based on finite element method (FEM) analysis that were used to investigate the machine's parameters [17]. Due to periodic symmetry only a quarter of the complete motor cross-section

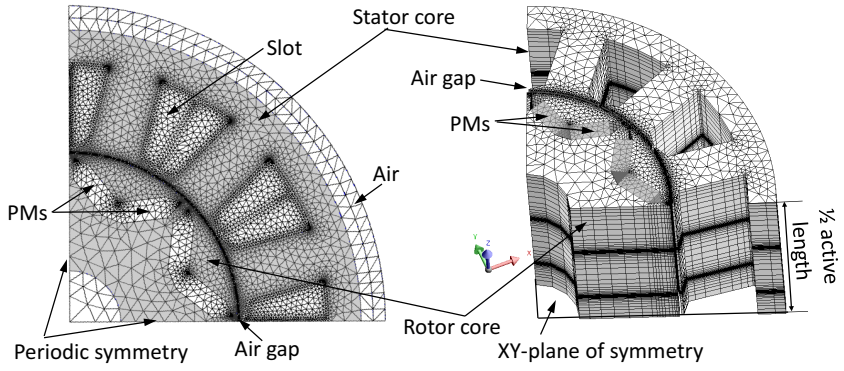

Fig. 3. Mesh descritization of the two-dimesional (a) and three-dimesional (b) finite element model together with symmetry planes (winding regionas were set to invisible)

is modeled circumferentially. Axial symmetry of the IPM motor allows the 3D FE model to be reduced to one eight of the overall machine volume. In the 2D FE model the mesh consists of 22 165 nodes and 10 762 elements, while in the 3D FE model consists of 181 581 nodes and 346 543 elements.

In transient analysis, the three-phase stator winding is fed by sinusoidal waveforms. Analysis of the loss distribution within the motor assembly was carried out using established discrete time step finite element modeling. Also, a three-dimensional FEM was then undertaken to account for the end-effects as well as axial segmentation of the permanent magnet. For eddy-current loss reduction within permanent magnets the IPM motor was designed with six segments of permanent magnets in an axial direction.

The variable electromagnetic torque profile at armature current is shown in Fig. 4(a). It can be seen that the higher the current, the more significant the torque ripple. Fig. 4(b) illustrates the linear dependence between the amplitude of the armature phase current circulating in the stator winding and the electromagnetic torque. The torque constant ranges from 0.67 to 0.72 Nm/Arms at an root mean square (RMS) current ranging from 53 to 163 A, respectively. The maximum current that can be fed to the winding is 230 A.

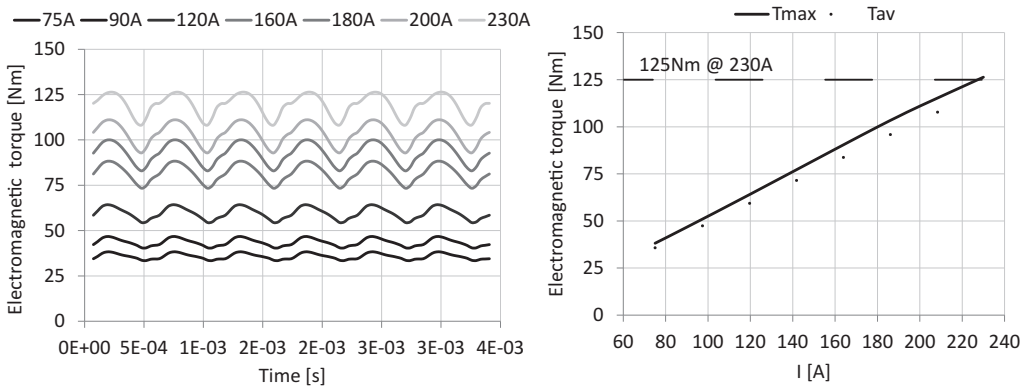

Fig. 4. Variation of electromagnetic torque vs. time at different armature currents (a) and torque vs. armature current (b). Results were obtained at a rotor speed of 4500 rpm at room temperature

For traction motor application, it is important for the electric machine to be characterized by low levels of vibration, noise, and speed fluctuations. The IPM motor designed and presented here is characterized by acceptable values of two components, torque ripple and cogging torque. The first one is caused mainly by fluctuations generated in the field distribution and the armature magnetomotive force (MMF); the second one is caused by the interaction between the stator air-gap permeance and the permanent magnet MMF [18]. At a low speed and at increasing current (see Fig. 4(a)), torque ripple can be observed; this effect may result in undesirable speed variations, leading in turn to acoustic noise and vibrations. The torque ripple coefficient for the analyzed IPM motor rose from 13.23 to 18.39% due to a current ranging from I = 75 A to I = 180 A, respectively. With a further increase in the current, the torque ripple coefficient decreased. The torque coefficient was computed according to the formula presented in [19].

Fig. 5 shows the variation of the cogging torque with respect to different rotor positions and the cogging torque harmonic analysis at low speeds. It was observed that the amplitude of the cogging torque is 0.978 Nm; its total harmonic distortion is THD = 59.57%. Because cogging torque is a very important factor in high performance and precision in electrical motors, harmonics reduction methods will be adopted in a future project for the prototype of the IPM motor presented in this paper.

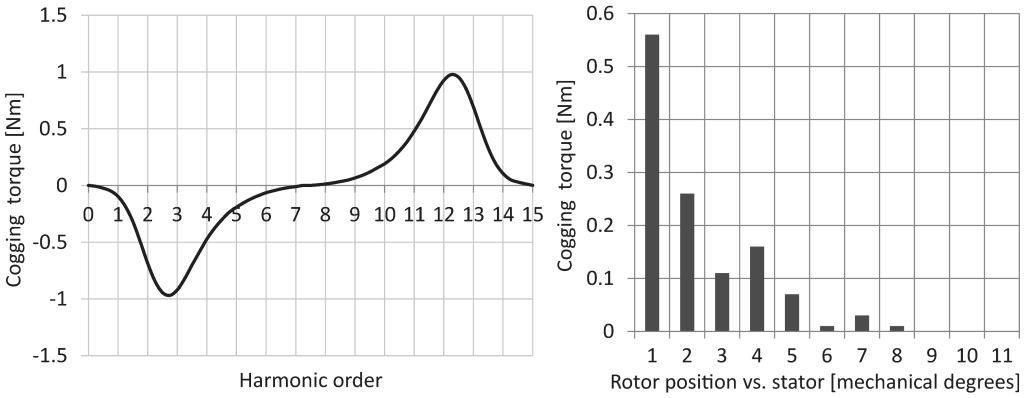

(a) (b)

Fig. 5. Cogging torque period (a) and its harmonic analysis (b) at a rotor speed of 1000 rpm at room temperature

The next major motor parameter is the no-load back-EMF characteristic, as shown in Fig. 6. Fig. 6(b) shows the harmonic analysis of back-EMF at 1000 rpm and THD = 7.47%. Based on RMS line-to-line back-EMF voltage, the constant voltage is 0.35 Vs/rad at 1000 rpm. At a base speed of 4500 rpm, the winding generates 135 V.

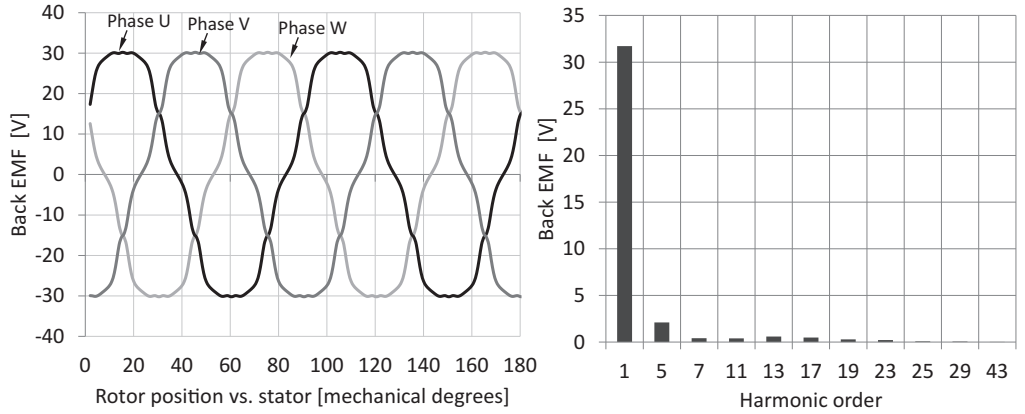

(a) (b)

Fig. 6. Line-to-neutral back-EMF waveforms during no-load operation at 1000 rpm

3. Eddy current loss analysis

A three-dimensional (3D) FEM was used for analysis of the loss distribution within the motor assembly and carried out using established discrete time step finite element modeling. The end effects, such as end-winding, and axial segmentation of the permanent magnets were taken into account in order to increase the accuracy of the eddy current loss computation. The motor's winding is star-configured, linked to an external circuit, excited from a three-phase symmetrical, and fed by a sinusoidal current source to represent the action of the inverter. At a maximum operating speed of 11 000 rpm the fundamental frequency of the 8-pole machine is 733.333 Hz.

The iron loss generated in the laminated core pack of the stator and rotor was computed using the established method of hysteresis, classic joule eddy, and excess loss components [17]:

$$P_{\mathrm{Fe}} = V_{\mathrm{Fe}}\left(k_h B_m^2 f + \sigma\frac{d^2}{12}\left(\frac{\mathrm{d}B}{\mathrm{d}t}(t)\right)^2 + k_e\left(\frac{\mathrm{d}B}{\mathrm{d}t}(t)\right)^{3/2}\right)k_f, \tag{1}$$

where: V_{Fe} is the volume of the meshed rotor/stator core taken into account for iron loss investigation, k_h is the hysteresis coefficient, B_m is the maximum of flux density excursion over an electrical cycle, f is the frequency, σ is the electric conductivity of the laminated rotor/stator steel, d is the thickness of a single sheet of lamination, k_e is the excess loss coefficient, and k_f is the packing factor of the laminated core pack. The loss parameters for the lamination steel used in the IPM prototype motor (M270-35A) are: $k_h = 93.89$ Ws/T^2/m^3, $k_e = 1.33$ W/(Ts^{-1})$^{3/2}$/m^3, $k_f = 0.98$, $d = 0.35$ mm, $\sigma = 2.22$ e6 (Ω^{-1}m).

Fig. 7 shows the no-load iron loss; it can be seen that the hysteresis and eddy current loss in the stator core are primary. The total stator and rotor iron losses on short circuit (three-phase winding short-circuit faults) at 4500 rpm are 160 and 132 W, respectively.

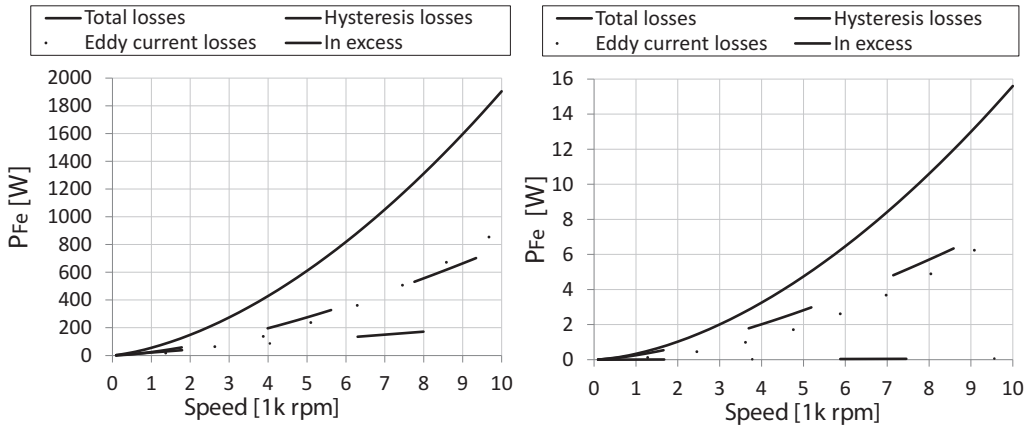

Fig. 7. No-load results of stator (a) and rotor (b) iron loss at no-load condition

At a nominal current of 228 A and a speed of 4500 rpm, the iron loss increased rapidly compared with no-load results at the same speed (Fig. 8). Moreover, the losses also increased

along with frequency. For example, at a maximum speed of 11 krpm, the total stator and rotor iron losses at nominal current were 4.8 and 0.68 kW, respectively.

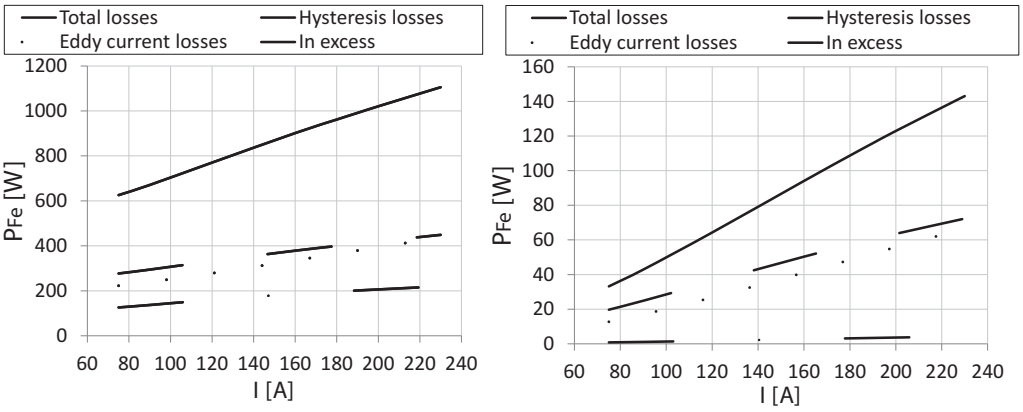

Fig. 8. Stator (a) and rotor (b) iron loss results vs. load operation at 4500 rpm

The power loss within the PMs is determined from the Joule loss [14]:

$$P_{\mathrm{PM}} = \iiint_V \boldsymbol{E} \cdot \boldsymbol{J}\,\mathrm{d}V = \rho \iiint_V \boldsymbol{J}^2\,\mathrm{d}V, \tag{2}$$

where: $\boldsymbol{E}$ is the electric field strength, $\boldsymbol{J}$ is the current density within the PM, and ρ is the resistivity of the PM.

The eddy current losses computed within magnets on an open- and short-circuit for different numbers of segments caused by a pole magnet at different speeds are shown in Fig. 9. As would be

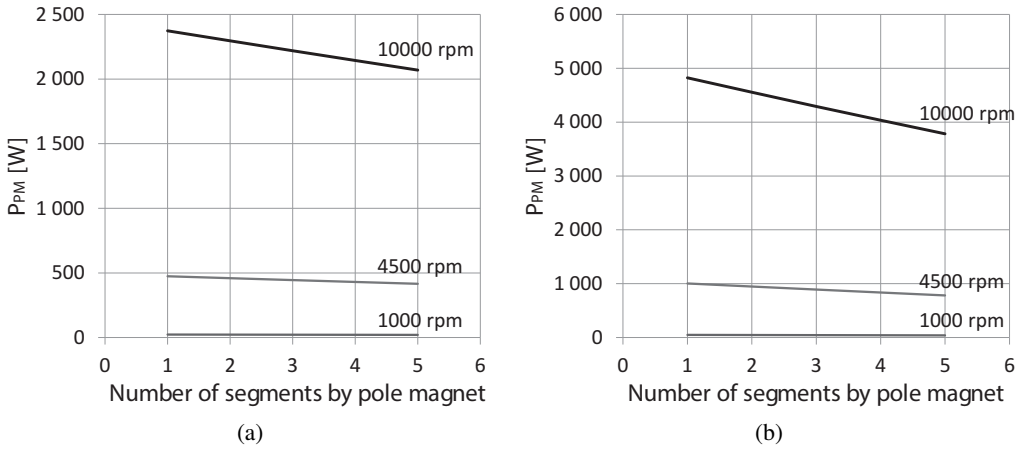

Fig. 9. PM eddy current loss on no-load (a) and SC (b) vs. number of segments by pole magnet

expected, axial segmentation led to a substantial reduction in the PM eddy current loss [20–22]. At load operation and at high speed, the magnet loss was only 13% after 5 segments were used per rotor pole. The number of segments must be increased for further reduction of eddy current loss.

The analyzed IPM motor may produce a significant copper loss with increases in frequency and temperature. The investigation of high-frequency effects in windings and their temperature dependency were analyzed in [23, 24]. The copper loss within the winding was determined from the winding resistance, which rises with winding temperature; it is very important to investigate this loss during the motor design process. The copper eddy current loss in the presented IPM prototype motor, and more measurement data will be investigated in a future project.

4. Collapse load analysis

The short-circuit current at collapse load is an important factor that cannot be ignored. The current amplitude can reach a very high value at the sub transient envelope; this can affect the lifetime of the machine's winding and increase the rotor/stator temperature, which may in turn increase the risk of demagnetization of the magnet. Moreover, the short-circuit fault in the stator winding may be reflected in the RMS values, the spectrum of stator current harmonics, and the harmonic spectrum of the electromagnetic torque [25–28]. Another important effect of this fault related to motor operation may concern unbalanced electromagnetic force in the rotor [25]. Based on the fundamental theory of a sudden three-phase short circuit [29, 30], the analytical model was built and verified in comparison to the numerical 2D FE model.

An equivalent circuit of a synchronous machine at a winding short-circuit fault is shown in Fig. 10. The voltage induced by the field winding flux $e(t)$ is the sum of the armature-resistance R voltage drop and of the voltage drop on the synchronous reactance X_s, where $X_s = \omega_e \cdot L_s$. The synchronous inductance was computed based on the operator reactance X_L and operator impedance Z. Using the following equations, the impedance, reactance, and synchronous inductance were computed:

$$\bar{Z} = \frac{E_m}{I_{SC}}, \tag{3}$$

$$\bar{X}_L = \sqrt{\left(\frac{E_m}{I_{SC}}\right)^2 - R^2}, \tag{4}$$

$$L_s = \frac{\bar{X}_L}{2\pi \cdot f_e}, \tag{5}$$

where E_m is the peak value of the induced phase voltage in the winding at no-load operation, computed from the FE model as input data; I_{SC} is the steady state short-circuit current, also provided from the FE model as input data; f_e is the electrical frequency; and ω_e is the angular speed.

The generated voltage in each terminal phase was computed starting from time $t = 0$ s:

$$e_U(t) = E_m \sin(2\pi \cdot f_e \cdot t + \varphi), \tag{6}$$

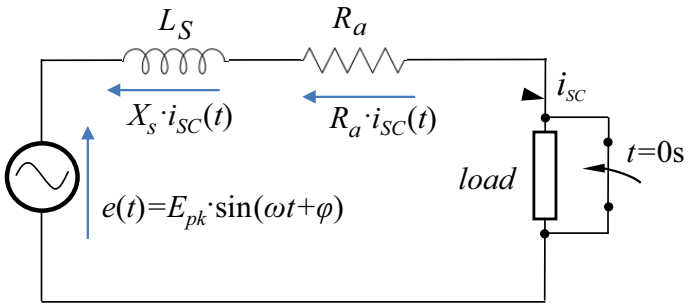

Fig. 10. Equivalent circuit of the synchronous machine with short applied at terminals

$$e_V(t) = E_m \sin\left(2\pi \cdot f_e \left(t + \frac{1}{3 \cdot f_e}\right) + \varphi\right), \tag{7}$$

$$e_W(t) = E_m \sin\left(2\pi \cdot f_e \left(t - \frac{1}{3 \cdot f_e}\right) + \varphi\right), \tag{8}$$

where φ is the initial rotor position angle of the generated armature voltage at time = 0 s. The main goal of the analytical analysis is to investigate collapse load; therefore, the torque constant k_t was used in the current waveform formulas, which are described by Equations (9)–(11). The machine operation is described by the load torque T_{load} before the short-circuit occurs. The collapse load simulates the machine trace of armature short-circuit currents in a synchronous machine after the winding fault occurs at a moment when the machine is operating at load condition. The adopted calculation methodology for the short-circuit currents assumes computation of SC currents at the time $t = 0$ s:

$$i_{SC,U}(t) = \sqrt{2} \cdot \frac{T_{\text{load}}}{k_t} \cdot \sin\left(2\pi \cdot f_e \cdot t + \varphi - \theta\right), \tag{9}$$

$$i_{SC,V}(t) = \sqrt{2} \cdot \frac{T_{\text{load}}}{k_t} \cdot \sin\left(2\pi \cdot f_e \left(t + \frac{1}{3 \cdot f_e}\right) + \varphi - \theta\right), \tag{10}$$

$$i_{SC,W}(t) = \sqrt{2} \cdot \frac{T_{\text{load}}}{k_t} \cdot \sin\left(2\pi \cdot f_e \left(t - \frac{1}{3 \cdot f_e}\right) + \varphi - \theta\right), \tag{11}$$

where θ is the angle of phase difference between voltage and current waveforms [20, 21]. The SC currents in the next iteration are defined as:

$$i_{SC}(t) = \mathrm{d}i(t) + i_{SC}(t - \mathrm{d}t), \tag{12}$$

where the incremental current is expressed by (13):

$$\mathrm{d}i(t) = \frac{(e(t - \mathrm{d}t) - R \cdot i_{SC}(t - \mathrm{d}t)) \cdot \mathrm{d}t}{L_s}. \tag{13}$$

The sub transient short-circuit peak current, computed by means of an analysis based on 2D finite element analysis (FEA), was equal to 700 A, whereas the peak value, computed using an

analytical spreadsheet, was 660 A (at $\varphi = 58°$ and $\theta = 0°$). The difference in the results is due to the end-winding inductance, which was not included in the analytical model. Nevertheless, since close agreement was achieved between the analytical and numerical analyses, the transient analysis was carried out via the solution of equations (9)–(13), whose results are presented below. Fig. 10 shows the waveforms of the 3-phase current under a short-circuit of the IPM motor run at starting load torque conditions equal to 0 and 125 Nm, respectively. All cases assume running at $\varphi = 58°$ of the initial angle position of back-EMF and the current waveform, as well as the torque electrical angle between stator and rotor flux linkage was set to $\theta = 0°$. At these parameters the machine reaches the highest value of short-circuit (SC) current.

Fig. 11(b) shows that the winding short-circuit fault occurred at the moment where the machine was running with load; this is one of the most critical faults in PM motor drives [30–34]. The AC current at the sub transient period is almost 2.8 and 3.6 times the steady-state fault current

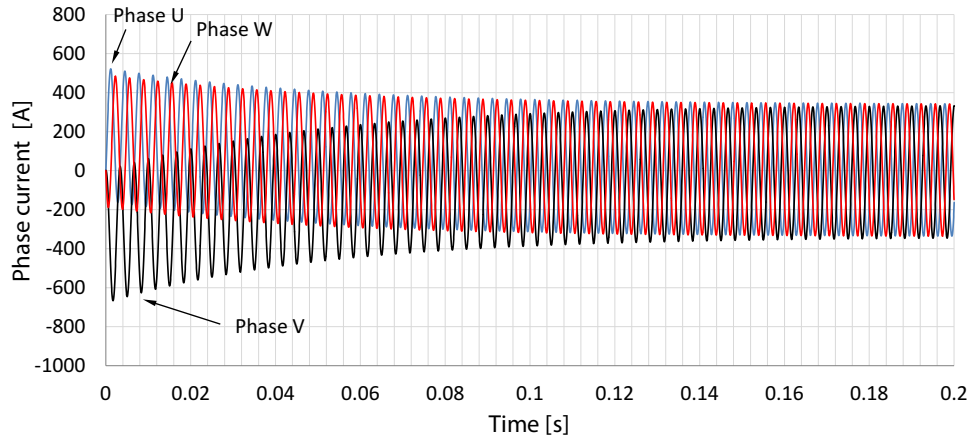

(a)

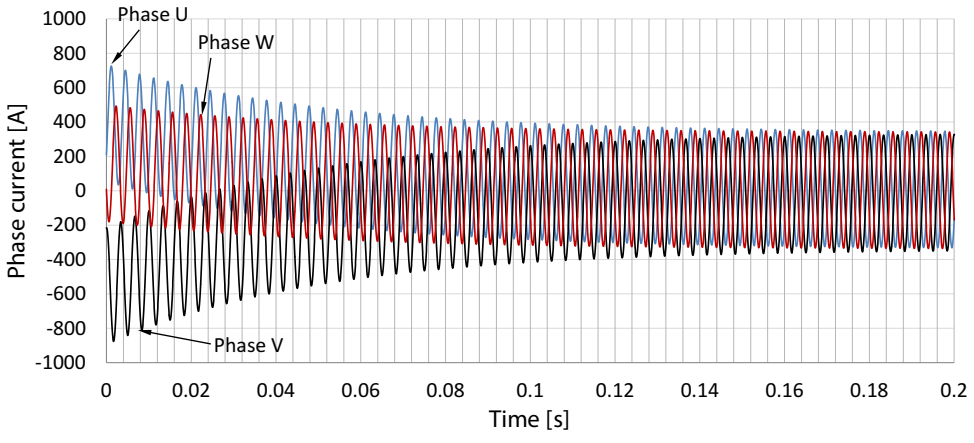

(b)

Fig. 11. Armature 3-phase short-circuit current on an initially unloaded synchronous machine (a) and at a nominal load of 125 Nm (b) after collapse load at a base speed of 4500 rpm

at non-loaded (0 Nm) and loaded torque (125 Nm), respectively. As can be seen from Fig. 11, the sub transient period lasts only for the first few cycles (here, up to 0.08 s), during which the current decrement is very rapid. During the transient period (starting from 0.08 s), the transient current is roughly 1.7 times the steady-state fault current in cases of both unloaded and loaded motors after the occurrence of the collapse load. It can be concluded that the collapse load which occurred in the machine at load operation may significantly prolong the sub transient period, leading to increased risk of a rise in temperature in the armature; therefore, in the rotor, the risk of demagnetization of the magnet may increase as well.

In order to demonstrate a SC current at torque loads ranging from 5 to 137 Nm and speeds ranging from 200 to 10 000 rpm, a map of the SC fault current is presented in Fig. 12.

	Speed [k rpm]																				
Torque [Nm]	0.2	0.5	0.6	0.8	1	1.5	1.75	2	2.5	2.75	3	3.5	3.75	4	4.5	5.5	6.5	7.5	8.5	9.5	10
137	626	772	792	820	837	861	869	874	882	885	887	891	892	894	896	899	901	903	904	905	905
133	619	762	782	809	826	849	857	862	870	872	875	878	880	881	883	886	888	890	891	892	892
124	612	752	771	798	814	837	844	850	857	860	862	866	867	868	870	873	876	877	878	879	879
117	606	744	763	789	805	828	835	840	847	850	852	856	857	858	860	863	865	867	867	869	869
115	605	742	761	787	803	825	832	837	845	847	850	853	854	856	858	860	863	864	865	866	866
108	598	732	751	775	791	814	820	825	832	835	837	840	842	843	845	848	850	851	852	853	853
100	592	722	740	764	780	802	808	813	820	822	824	828	829	830	832	835	837	838	839	840	840
83	578	702	719	742	757	778	784	788	795	797	799	802	804	805	807	809	811	812	813	814	814
75	571	692	709	731	746	766	772	776	782	785	787	790	791	792	794	796	798	799	800	801	801
66	564	682	698	720	734	754	759	764	770	772	774	777	778	779	781	783	785	786	787	788	788
60	558	672	688	709	723	742	747	751	757	760	762	764	766	767	768	770	772	773	774	775	775
53	551	662	678	698	711	730	735	739	745	747	749	752	753	754	755	758	759	760	761	762	762
43	544	652	667	687	700	718	723	727	733	735	736	739	740	741	743	745	747	747	748	749	749
35	538	642	657	676	689	706	711	715	720	722	724	726	727	728	730	732	734	735	735	736	736
24	531	632	646	665	677	694	699	702	708	710	711	714	715	716	717	719	721	722	722	723	723
20	524	622	636	654	666	682	687	690	695	697	699	701	702	703	704	706	708	709	709	710	710
14	517	612	626	643	654	670	674	678	683	685	686	688	689	690	692	693	695	696	696	697	697
5	511	602	615	632	643	658	662	666	670	672	674	676	677	678	679	681	682	683	683	684	684

Fig. 12. SC fault current map of different load torques and speeds. The results were obtained at $\varphi = 58°$ and $\theta = 0°$. The dark bars represent the highest values of the SC currents

5. Conclusions and recommendations

The paper presents the electromagnetic review of a radial flux IPM motor with a V-shaped permanent magnet. The 80-kW prototype of an IPM motor built for this purpose yielded satisfactory results for useful machine parameters such as torque constant and voltage constant. Moreover, a required electromagnetic torque of 125 Nm (at the maximum current at which the winding can be fed) was achieved. Three-phase short-circuit faults demonstrate that the peak sub transient current rises very rapidly along with the load operation. It is strongly recommended that electric motor designers should develop a well-built design taking into account all possible damage during SC. Due to a very high SC current at high speed and at high torque load, the physical machine parameters may significantly increase the risk of PM demagnetization (see Fig. 12). It can also be concluded that collapse load may increase the transient torque peak value compared to steady state values, which may in turn reduce the lifetime of, e.g., the windings. It is also recommended that transient analysis of torque load during SC should be taken into account at motor design.

Acknowledgements

The project "Development of the control system and BLDC /PMSM electric motor as part of the research and development of Auto Power Electronic Piotr Skrobotowicz" financed by co-financing from RPO WV 2014–2020, Innovations in enterprises, project number RPOP.01.01.00-16-0015/16.

References

[1] Liu H., Chen X., Wang X., *Overview and prospects on distributed drive electric vehicles and its energy saving strategy*, Przeglad Elektrotechniczny, no. 7a, pp. 122–125 (2012).

[2] Soleimani J., Vahedi A., *IPM synchronous motor for traction applications: Performance analysis considering airgap variation*, Przegląd Elektrotechniczny, no. 12a, pp. 200–205 (2012).

[3] Glinka T., Bernatt J., *Asynchronous slip-ring motor synchronized with permanent magnets*, Archives of Electrical Engineering, vol. 66, no. 1, pp. 199–206 (2017).

[4] Lyskawinski W., Jedryczka C., Stachowiak D., *Analysis of 6-pole IPM synchronous motor with tangential magnets using finite element method*, Przegląd Elektrotechniczny, no. 4, pp. 34–37 (2016).

[5] Hongbo Q., Wenfei Y., Cunxiang Y., Ran Y., *Influence of different rotor magnetic circuit structure on the performance of permanent magnet synchronous motor*, Archives of Electrical Engineering, vol. 66, no. 3, pp. 583–594 (2017).

[6] Nobuyoshi M., *Front-and-rear-wheel-independent-drive-type electric vehicle (FRID EV) with compatible driving performance and safety*, EVS24 International Battery, Hybrid and Fuel Cell Electric Vehicle Symposium, Stavanger, Norway, vol. 1, no. 1, pp. 17–26 (2009), DOI: 10.3390/wevj3010017.

[7] Murata S., *Innovation by in-wheel-motor drive unit*, Vehicle System Dynamics, vol. 50, no. 6, pp. 807–830 (2012).

[8] Sun Y., Li M., Liao C., *Analysis of wheel hub motor drive application in electric vehicles*, MATEC web if Conferences 100, Vehicle System Dynamics, pp. 1–6 (2017), DOI: 10.1051/matecconf/201710001004.

[9] Hwang M.H., Han J.H., Kim D.H., Cha H.R., *Design and analysis of rotor shapes for IPM motors in EV Power Traction Platforms*, Energies, vol. 11, no. 10, pp. 1–12 (2018), DOI: 10.3390/en11102601.

[10] Lim S., Min S., Hong J.P., *Optimal rotor design of IPM motor for improving torque performance considering thermal demagnetization of magnet*, IEEE Transactions on Magnetics, vol. 51, no. 3, pp. 1–5 (2015).

[11] Kim Y.H., Lee S.S., Cheon B.C., Lee J.H., *Study on optimal design of 210 kW traction IPMSM considering thermal demagnetization characteristics*, AIP Advances, vol. 8, iss. 4. pp. 1–13 (2013), DOI: 10.1063/1.4994160.

[12] Fang L., Hong J.P., *Flux-barrier design technique for improving torque performance of interior permanent magnet synchronous motor for driving compressor in HEV*, 5th IEEE Vehicle Power and Propulsion Conference (VPPC), pp. 1486–1490 (2009), DOI: 10.1109/VPPC.2009.5289547.

[13] Mirazimi M.S., Kiyoumarsi A., *Magnetic field analysis of Multi-flux-barrier interior permanent-magnet motors through conformal mapping*, IEEE Transactions on Magnetics, vol. 53, no. 12, pp. 1–12 (2017).

[14] Lim S., Min S., Hong J.P., *Shape design optimization of interior permanent magnet motor for vibration mitigation using level set method*, International Journal of Automotive Technology, vol. 17, no. 5, pp. 917–922 (2016).

[15] Kim S.I., Lee G.H., Lee J.J., Hong J.P., *Simple design approach for improving characteristics of interior permanent magnet synchronous motors for electric air-conditioner system in HEV*, International Journal of Automotive Technology, vol. 11, no. 2, pp. 277–282 (2010).

[16] Liu X., Li Y., Liu Z., Ling T., Luo Z., *Optimized design of a high-power-density PM-assisted synchronous reluctance machine with ferrite magnets for electric vehicles*, Archives of Electrical Engineering, vol. 66, no. 2, pp. 279–293 (2017).

[17] *Flux 3D, User's Manual*, Cedrat, France, January (2019).

[18] Mattavelli P., Tubiana L., Zigliotto M., *Torque-ripple reduction in PM synchronous motor drives using repetitive current control*, IEEE Transactions on Power Electronics, vol. 20, no. 6, pp. 1423–1431 (2005).

[19] Awah C.C., Okoro O.I., Chikuni E., *Cogging torque and torque ripple analysis of permanent magnet flux-switching machine having two stators*, Archives of Electrical Engineering, vol. 68, no. 1, pp. 115–133 (2019).

[20] Yamazaki K., Fukushima Y., Sato M., *Loss analysis of permanent-magnet motors with concentrated windings-variation of magnet eddy-current loss due to stator and rotor shapes*, IEEE Transactions on Industry Applications, vol. 45, no. 4, pp. 1334–1342 (2009).

[21] Yamazaki K., Abe A., *Loss analysis of interior permanent magnet motors considering carrier harmonics and magnet eddy currents using 3-D FEM*, IEEE International Electric Machines and Drives Conference, May 3-5 Antalya, Turkey, pp. 904–909 (2007), DOI: 10.1109/IEMDC.2007.382794.

[22] Oh S.Y., Cho S.Y., Han J.H., Lee H.J., Ryu G.H., Kang D., Lee J., *Design of IPMSM rotor shape for magnet eddy-current loss reduction*, IEEE Transactions on Magnetics, vol. 50, no. 2, pp. 841–844 (2014).

[23] Mellor P.H., Wrobel R., McNeill N., *Investigation of proximity losses in a high speed brushless permanent magnet motor*, IEEE Industry Applications Society 41st Annual Meeting, pp. 1514–1518 (2006), DOI: 10.1109/IAS.2006.256730.

[24] Wrobel R., Mlot A., Mellor P.H., *Investigation of end-winding proximity losses in electromagnetic devices*, XIX International Conference on Electrical Machines (ICEM), pp. 1–6 (2010), DOI: 10.1109/ICELMACH.2010.5608236.

[25] Constantin A., Fireteanu V., Leconte V., *Effects of the short-circuit faults in the stator winding of induction motors and fault detection through the magnetic field harmonics*, The International Symposium on Advanced Topics in Electrical Engineering, May 23-25, Bucharest, Romania, pp. 1–6 (2013), DOI: 10.1109/ATEE.2013.6563386.

[26] Rahnama M., Nazarzadeh J., *Synchronous machine modelling and analysis for internal faults detection*, IEEE International Electric machines and Drives Conference, Antalya, Turkey, pp. 1–6 (2007), DOI: 10.1109/IEMDC.2007.382812.

[27] Li G.J., Hloui S., Ojeda J., Hoang E., Lecrivain M., Gabsi M., Zhu Z.Q., *Excitation winding short-circuit in hybrid excitation permanent magnet motor*, IEEE Transactions on Energy Conversion, vol. 29, no. 3, pp. 567–575 (2014).

[28] Eklund P., Eriksson S., *Winding design independent calculation method for short circuit current in permanent magnet synchronous machines*, XIII International Conference on Electrical Machines (ICEM), October 25, Alexandroupolis, Greece, pp. 1–6 (2018), DOI: 10.1109/ICELMACH.2018.8506920.

[29] *IEEE Recommended Practice for Calculating Short-Circuit Currents in Industrial and Commercial Power Systems*, The Institute of Electrical and Electronics Engineers, Inc., new York, USA, ISBN 0738149322, 9780738149325 (2006).

[30] Fitzgerald A.E., Charles Kingsley Jr., Umans S., *Electric Machinery. Fourth edition*, McGraw-Hill Book Company, New York (1983).

[31] Husain I., Anwa M.N., *Fault analysis of switched reluctance motor drives*, IEEE International Electric Machines and Drives Conference (IEMDC), Seattle, WA, USA, pp. 41–43 (1999), DOI: 10.1109/IEMDC.1999.769021.

[32] Eilenberger A., Schrodl M., *Sudden short-circuit analysis of a salient permanent magnet synchronous machine with buried magnets for traction applications*, Proceedings of 14^{th} International Power Electronics and Motion Control Conference (EPE-PEMC), Ohrid, Macedonia, pp. 117–120 (2010), DOI: 0.1109/EPEPEMC.2010.5606596.

[33] Najafi S., *Coupled electromagnetic-thermal problems in electrical energy transducers*, PhD Thesis, Faculty of Graduate and Research through Electrical and Computer Engineering, University of Windsor, Windsor, Ontario, Canada (2006).

[34] Chen Y., Zhang B., *Minimization of the electromagnetic torque ripple caused by the coils inter-turn short circuit in dual redundancy permanent magnet synchronous motors*, Energies, vol. 10, no. 11, pp. 1–23 (2017), DOI: 10.3390/en10111798.